Electronic band structure for occupied and unoccupied states of the natural topological superlattice phase Sb_2Te

L. Khalil,[1,2] E. Papalazarou,[1] M. Caputo,[1] N. Nilforoushan,[1] L. Perfetti,[3] A. Taleb-Ibrahimi,[2] V. Kandyba,[4] A. Barinov,[4] Q. D. Gibson,[5] R. J. Cava,[5] and M. Marsi[1]

[1]*Laboratoire de Physique des Solides, CNRS, Univ. Paris-Sud, Université Paris-Saclay, 91405 Orsay Cedex, France*

[2]*UR1-CNRS/Synchrotron SOLEIL, Saint Aubin BP 48, Gif-sur-Yvette F-91192, France*

[3]*Laboratoire des Solides Irradiés, Ecole Polytechnique, CNRS, CEA, Université Paris-Saclay, 91128 Palaiseau Cedex, France*

[4]*Elettra – Sincrotrone Trieste SCpA, AREA Science Park, 34149 Trieste, Italy*

[5]*Department of Chemistry, Princeton University, Princeton, New Jersey 08544, USA*

(Received 18 November 2016; published 15 February 2017)

We present an experimental study describing the effects of surface termination on the electronic structure of the natural topological superlattice phase Sb_2Te. Using scanning angle-resolved photoemission microscopy, we consistently find various nonequivalent regions on the same surface after cleaving various Sb_2Te single crystals. We were able to identify three distinct terminations characterized by different Sb/Te surface stoichiometric ratios and with clear differences in their band structure. For the dominating Te-rich termination, we also provide a direct observation of the excited electronic states and of their relaxation dynamics by means of time-resolved angle-resolved photoemission spectroscopy. Our results clearly indicate that the surface electronic structure is strongly affected by the bulk properties of the superlattice.

DOI: 10.1103/PhysRevB.95.085118

I. INTRODUCTION

Three-dimensional topological insulators (3D TIs) constitute a novel state of quantum matter supporting spin-polarized metallic surface states while their bulk is insulating [1–4]. These surface states are topologically protected and have a Dirac cone dispersion with a special spin texture, as it has been extensively demonstrated for prototype compounds like Bi_2Se_3 and Bi_2Te_3 [5,6]. The particular properties of the robust topological surface states (TSSs) of these materials result from the combined action of a strong spin-orbit coupling and of time-reversal symmetry, which ensures the crossing of the energy levels of surface states at specific points in the Brillouin zone (Kramers theorem) and prevents backscattering of surface electrons in the presence of nonmagnetic impurities [7,8]. All these features make TIs fascinating and promising candidates for a new generation of electronic and spintronic devices [9], and are triggering novel efforts to be able to tune and engineer the TSSs band structure.

In this context, various theoretical studies have anticipated that multilayer structures, composed of an ordered stacking sequence of TIs interleaved with other compounds, sandwiched in a superlattice, present new topological properties [10,11]. More recently, a theoretical and experimental study has indicated that the natural superlattice series $(Sb_2)_m$-Sb_2Te_3 ($m = 0$–3), made of an ordered stacking of integer numbers of Sb_2 bilayers (BLs) and Sb_2Te_3 quintuple layers (QLs), possesses tunable TSSs for the whole range $m = 0$–3, with the surface termination playing a key role [12].

We hereby focus our attention on the most representative material in the topological superlattice series $(Sb_2)_m$-Sb_2Te_3, namely, diantimony tellurium Sb_2Te ($m = 2$). This particular compound is made of two Sb_2 BLs interleaved with five-layer stacks of Sb_2Te_3 [13,14] [see Fig. 1(a)]. Sb_2Te_3 is a member of the series ($m = 0$), and its electronic structure has already been investigated both experimentally and theoretically [6,12,15–17]. After cleaving a Sb_2Te single crystal, three different surfaces can be obtained [see Fig. 1(a)], specifically, a "Sb-rich 1BL" termination obtained after breaking the van der Waals bonds between the two Sb_2 BLs, a "Sb-rich 2BLs" termination envisaged upon breaking the van der Waals bonds to a neighboring Sb_2Te_3 QL, and a "Te-rich QL" termination resulting from breaking the interaction between the building blocks [12]. Previous results suggest that these three distinct surface terminations are actually simultaneously present on real cleaved surfaces of Sb_2Te, but a clear evidence of their coexistence and a precise description of their properties has not been provided yet. The relevance of this issue for the overall properties of the system calls for more detailed experimental studies of the interplay between surface terminations of Sb_2Te and its electronic properties.

In this work, we characterize the three surface terminations of Sb_2Te via microscopic x-ray photoemission spectroscopy and angle-resolved photoemission spectroscopy (μ-XPS and μ-ARPES), providing also a direct visualisation of the ultrafast transient carrier population after photoexcitation using time-resolved angle-resolved photoemission spectroscopy (trARPES). The combination of these experimental techniques gives access to thus far missing information on both the occupied and unoccupied electronic band structure of Sb_2Te.

II. METHOD AND EXPERIMENTAL DETAILS

High-quality single crystals of Sb_2Te [18] were cleaved *in situ* with a top-post under UHV conditions (base pressure better than 2.5×10^{-10} mbar), and were measured with μ-XPS, μ-ARPES, and trARPES.

The μ-XPS and μ-ARPES experiments were performed on the Spectromicroscopy beamline at the Elettra synchrotron light source, using photons with an energy of 74 eV. The incident photon beam was linearly P polarized and focused down to a submicrometric spot ($\sim$0.6 μm in diameter) on the sample surface using a Schwarzschild objective. The photo-

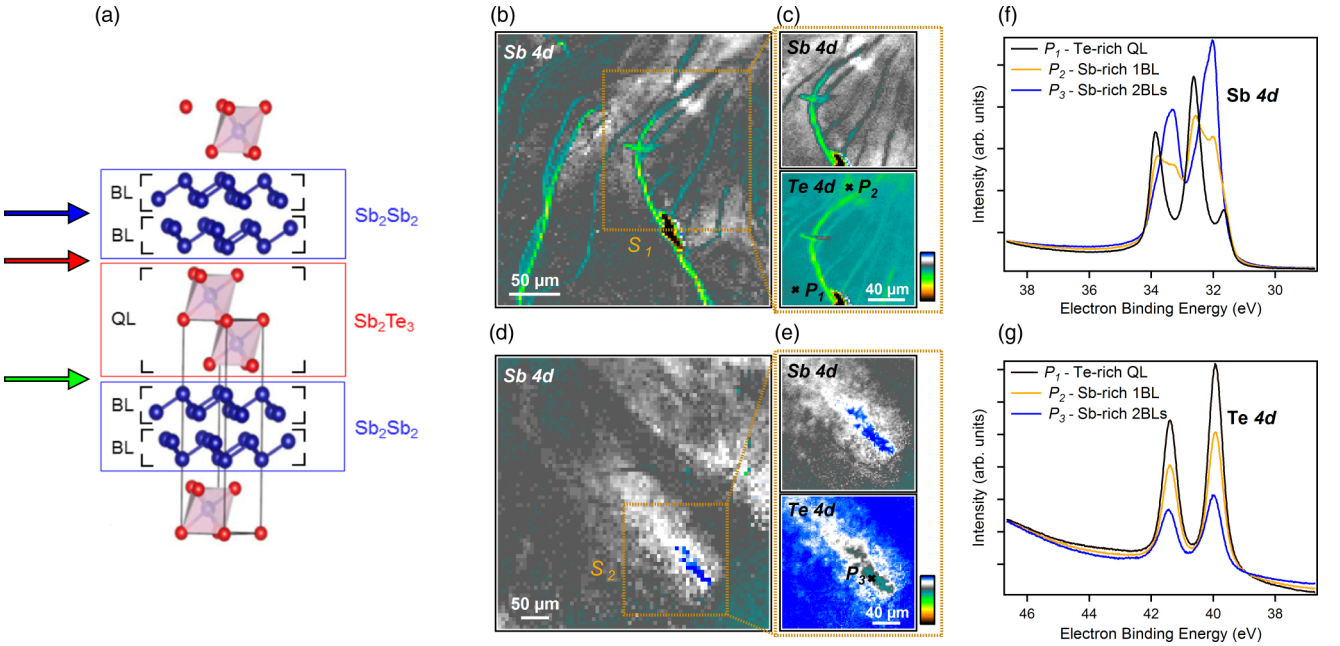

FIG. 1. Crystal structure of Sb_2Te and scanning photoemission microscopy images and spectra taken at a photon energy of 74 eV. (a) Crystal structure of Sb_2Te showing both Sb_2Te_3 QL and Sb_2 BLs building blocks [14]; horizontal arrows indicate the different cleaving planes. (b) SPEM image, recorded at photoelectron kinetic energy corresponding to Sb 4*d* core level for the first cleave, revealing two terminations marked in white and gray intensity color scale; the S_1 box includes both terminations. (c) Upper and lower panel present higher resolution images of the S_1 regions, obtained at two distinct photoelectron kinetic energies corresponding to the Sb 4*d* and Te 4*d* core levels, respectively. The two images present reversed chemical contrast. (d) Sb 4*d* SPEM image for another cleaved surface, clearly revealing a third kind of termination (appearing as blue in the image), contained in the S_2 contour defining the third terminated surface. (e) Same as (c) but for the S_2 region. (f, g) Photoemission spectra of the Sb 4*d* and Te 4*d* core levels, obtained from points P_1, P_2, and P_3 and representative of the three coexisting terminations.

electrons were detected with energy and angular resolutions of 50 meV and $\pm 0.3^\circ$, respectively, by means of an internal movable hemispherical electron energy analyzer mounted on a precision two-axes goniometer setup [19].

The trARPES measurements were performed using the FemtoARPES experimental setup, where pump-probe photoemission experiments can be performed with an energy resolution of 60 meV and a temporal resolution of 80 fs. Photoelectrons were excited with 6.32 eV photons, obtained as the fourth harmonic generated by cascade frequency mixing in BBO crystals (β-BaB_2O_4) from the 1.58-eV laser that is also used to pump the transient populated states and bands in a pump-probe configuration. (A detailed description of our experimental setup can be found in [20,21].) The use of a 6.32-eV probe gives access to a limited portion of k space but is sufficient in this case to observe the unoccupied TSSs. The out-of-equilibrium spectra were recorded using linear *S*-polarized 6.32-eV photons and were collected under incident pump fluence of 0.28 mJ/cm^2. All measurements were carried out at a base temperature of 110 K.

III. RESULTS AND DISCUSSION

The scanning photoemission microscopy (SPEM) measurements were performed combining the two operating modes of the instrument: (i) imaging, where the specimen surface is mapped detecting photoelectrons in a selected kinetic energy window, and (ii) μ-XPS and μ-ARPES. All images were background subtracted and normalized to correct for topographic effects [22]. In Figs. 1(b) and 1(d), we present two typical SPEM images, obtained on two different cleaved surfaces by detecting photoelectrons in the XY-WZ window, corresponding to the Sb 4*d* core levels. In order to investigate in more detail their properties, we selected two specific regions: S_1 [Fig. 1(b)] and S_2 [Fig. 1(d)], delimited by dashed contours. In Fig. 1(c), we present a comparison of the images obtained from the S_1 region by measuring photoelectrons from the Sb 4*d* core level (upper panel) and from the Te 4*d* core level (lower panel). The reversed chemical contrast [23] between the two images makes it possible to directly identify the lateral variation of the Sb/Te stoichiometric ratio at the surface, and consequently the distribution of different surface terminations. In particular, the areas where the Sb/Te ratio is higher (more intensity in the upper panel and less intensity in the lower one) indicate a Sb-rich termination, while areas where the Sb/Te ratio is lower (less intensity in the Sb 4*d* image and more intensity in the Te 4*d* image) are typical of a Te-rich termination. In Fig. 1(e), we present a similar comparison for the Sb 4*d* and Te 4*d* microscopic concentration distributions within the S_2 region. Notably, we detect a microscopic area where the Sb/Te ratio is particularly high (blue in the Sb 4*d* maps), considerably higher with respect to the values obtained in the region S_1.

The coexistence of different types of surface terminations is further confirmed by analyzing the photoemission spectra of the Sb 4*d* and Te 4*d* shallow core levels [Figs. 1(f)

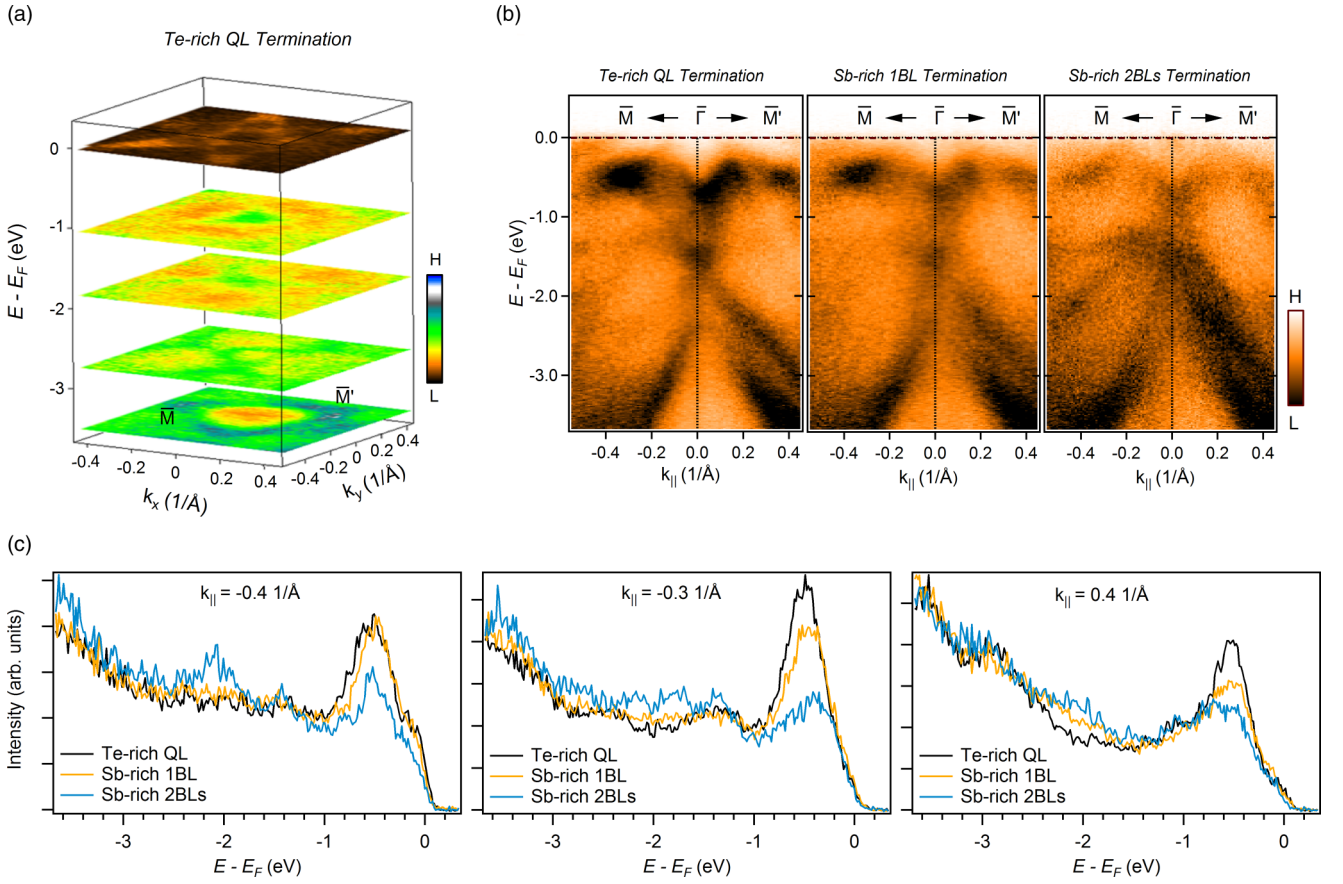

FIG. 2. Occupied electronic band structure of Sb_2Te. (a) Constant energy cuts for the Te-rich termination showing the Fermi surface topography and presenting the high-symmetry direction $\overline{\Gamma M}$–$\overline{\Gamma M'}$. (b) Intensity maps of photoelectrons, emitted for parallel wave vector along the $\overline{\Gamma M}$–$\overline{\Gamma M'}$ direction for the three microscopic regions, corresponding to points P_1, P_2, and P_3 in Fig. 1. (c) Energy distribution curves from the same microscopic regions for $k = -0.4\,\text{Å}^{-1}$ (left), $k = -0.3\,\text{Å}^{-1}$ (center), and $k = 0.4\,\text{Å}^{-1}$ (right panel).

and 1(g)] taken from three specific points P_1, P_2, and P_3 [Figs. 1(c) and 1(e)], representative of the distinct microscopic termination domains. The comparison of the stoichiometric concentration becomes more straightforward by looking at the core-level photoemission yield [24]: in particular, the Sb 4*d*/Te 4*d* intensity ratios (1.56, 2.54, and 4.86) from the regions represented by the three points P_1, P_2, and P_3 are consistent with an assignment to the three surface terminations: Te-rich QL, Sb-rich 1BL, and Sb-rich 2BLs, respectively. It is worth noting that the Sb 4*d* line shape varies depending on the surface termination: we can, in fact, detect three components for the peak corresponding to three chemical inequivalent Sb species. The first one, at higher binding energy, corresponds to the Sb atoms embedded in the Sb_2Te_3 QL, while the other two correspond to the Sb atoms in the Sb_2 BL. Their intensity ratio varies according to their distance from the surface: in the case of Sb_2Te_3 QL termination the highest binding energy component becomes predominant, while it becomes the faintest in the case of the Sb_2 BL termination. Furthermore, a quantitative analysis of the lateral distribution of the three different terminations in the SPEM images indicates that the Te-rich termination is the dominating one when cleaving the specimen.

Further information on the correlation between surface terminations and electronic properties could be obtained by operating the instrument in μ-ARPES mode. Figure 2(a) shows selected momentum dispersion images at different binding energies from a Sb_2Te_3 QL termination. The measured Fermi surface clearly shows the order three symmetry of Sb_2Te and makes it possible to identify the high-symmetry points M and M′ of the surface Brillouin zone. In Fig. 2(b), we compare the photoelectron intensity maps obtained along $\overline{\Gamma M}$–$\overline{\Gamma M'}$ for the three points P_1, P_2, and P_3, and in Fig. 2(c) we present energy distribution curves from the same microscopic regions and for selected wave vectors. The μ-ARPES yields clearly indicate that the projected band structures significantly differ from one surface termination region to another: in particular, moving from the Te-rich QL to the Sb-rich 2BLs termination, we can see the bands closer to the Fermi level becoming fainter, while the bands between 1 eV and 2 eV along $\overline{\Gamma M}$ become more intense. This could be due to the different relative weight of these states in the two sub-blocks constituting the superlattice: the former with a higher weight in the Sb_2Te_3 QL block, the latter with a higher weight in the Sb_2 BL block.

It should be noted that one of the most interesting Sb_2Te features, i.e., the TSSs, are located above the Fermi level [12], making them inaccessible using synchrotron-based ARPES. To overcome this issue, we used time-resolved ARPES: with this technique, pump photons excite hot electrons into

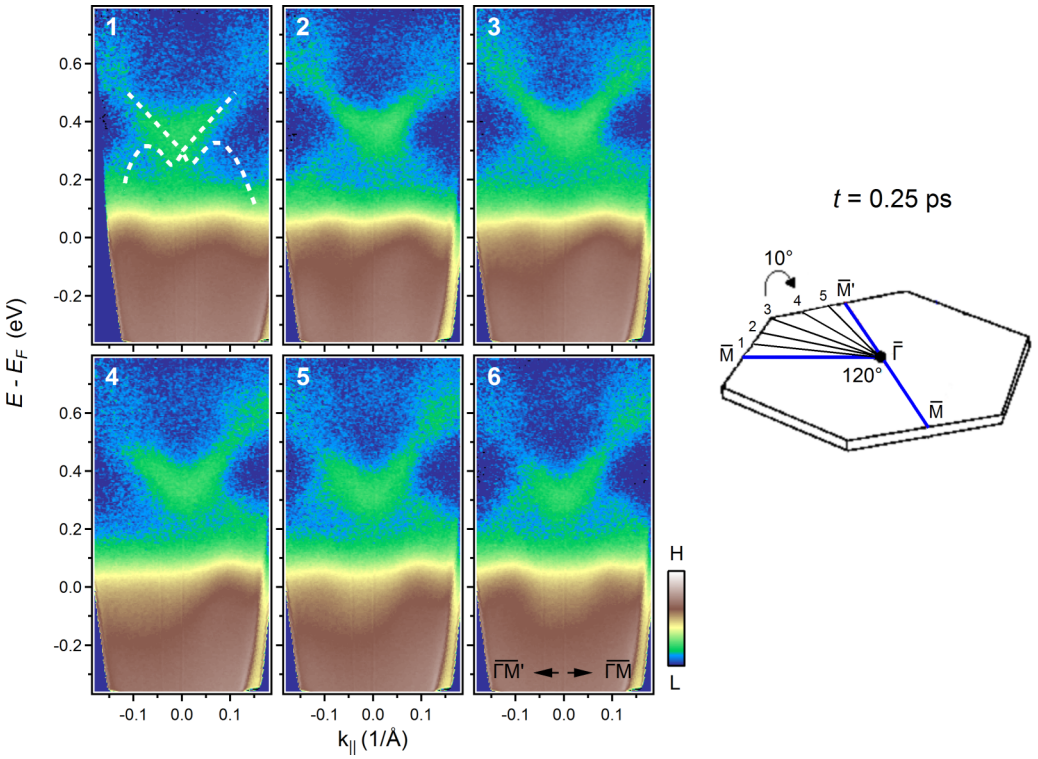

FIG. 3. Time-resolved ARPES sequence acquired after photoexcitation from the pump pulses for Sb_2Te. The color intensity is presented in logarithmic scale to make the signal from the unoccupied electronic states more evident. The intensity maps have been extracted at emission angles near $\bar{\Gamma}$, every 10 deg, at +0.25 ps pump-probe time delay.

the empty states, giving access to the band structure and the time evolution of the transient electron population. We explored various k-space directions in the surface Brillouin zone (in Fig. 3, we present results obtained at a pump-probe delay $t = 0.25$ ps), revealing the dispersion of the empty states: the white dashed line indicates the dispersion of the TSSs. Also, in the unoccupied bulk conduction band (BCB), we retrieve the threefold symmetry of the occupied states. The signal in the trARPES experiment comes mainly from the Te-rich QL termination, because the spot size of the probe beam (approximately 50 μm diameter) is considerably larger than the typical domain size for the other terminations.

In Fig. 4(a), we report the evolution of the ARPES yield acquired along the $\overline{\Gamma M}$–$\overline{\Gamma M'}$ high-symmetry direction at various pump-probe time delays following the ultrafast optical pump excitation. The images presented here are differences between positive and negative time delays, corresponding to excess carriers (electrons in red, and holes in blue). In the upper-left corner of Fig. 4, we display a schematic view of the bulk bands and the TSSs that can be used as a guide to the eye to interpret our experimental results. Because Sb_2Te is an intrinsically p-doped semimetal, the bulk valence band (BVB) crosses the Fermi level. At negative time delays—corresponding to a real delay of about 4 μs, i.e., to a complete relaxation of the system—we probe the electronic band structure in its ground state. Thus, the photoelectron intensity map taken at −0.10-ps time delay shows the TSSs and BCB unoccupied, at equilibrium. Immediately after the pump photoexcitation from the BVB at $t = 0$ ps, the first transient populated feature is the BCB located at $E - E_F = 0.5$ eV. Notice that at zero delay, the TSSs are only marginally populated, because they cannot be directly photoexcited. To follow the relaxation processes, we studied as a function of time delay the photoemission yield from different k-E integration windows, as indicated for the $t = 0.10$-ps time delay in Fig. 4(a), and corresponding to the unoccupied TSSs, BCB, and BVB, and to the occupied BVB [see Fig. 4(b)]. We can clearly notice that the primary maximum of the photoexcited electron population observed in the BCB (for window number 1 at $t = 0.10$ ps) is at about 50 fs, whereas the other regions attain their maxima only later; as already found in other similar cases, the initial photoexcitation into the BCB triggers a cascade of intraband and interband scattering processes towards low-lying states both in the BCB and TSSs [25,26].

Quantitatively, the characteristic lifetime of the excess electron population for the 1–8 k-E windows varies from $\tau_1 = 110$ fs (for window BCB1) to $\tau_8 = 330$ fs (for window BCB8). (These values are extracted by fitting our data with a single exponential.) It takes about 150 fs for the TSSs to reach their maximum population. The excess electrons in the TSSs relax through the BVB, thanks to their strong interband scattering processes and decay with average lifetime of about 560 fs. It should also be pointed out that the time evolution of the excess populations in the BVB is very well balanced for electrons and holes at all time delays, and the characteristic decay time for the relaxation of the BVB is 755 fs. As thoroughly discussed in previous studies, the relaxation of the TSSs and bulk bands is due to various processes, including intra- and interband scattering, with the electron-phonon scattering

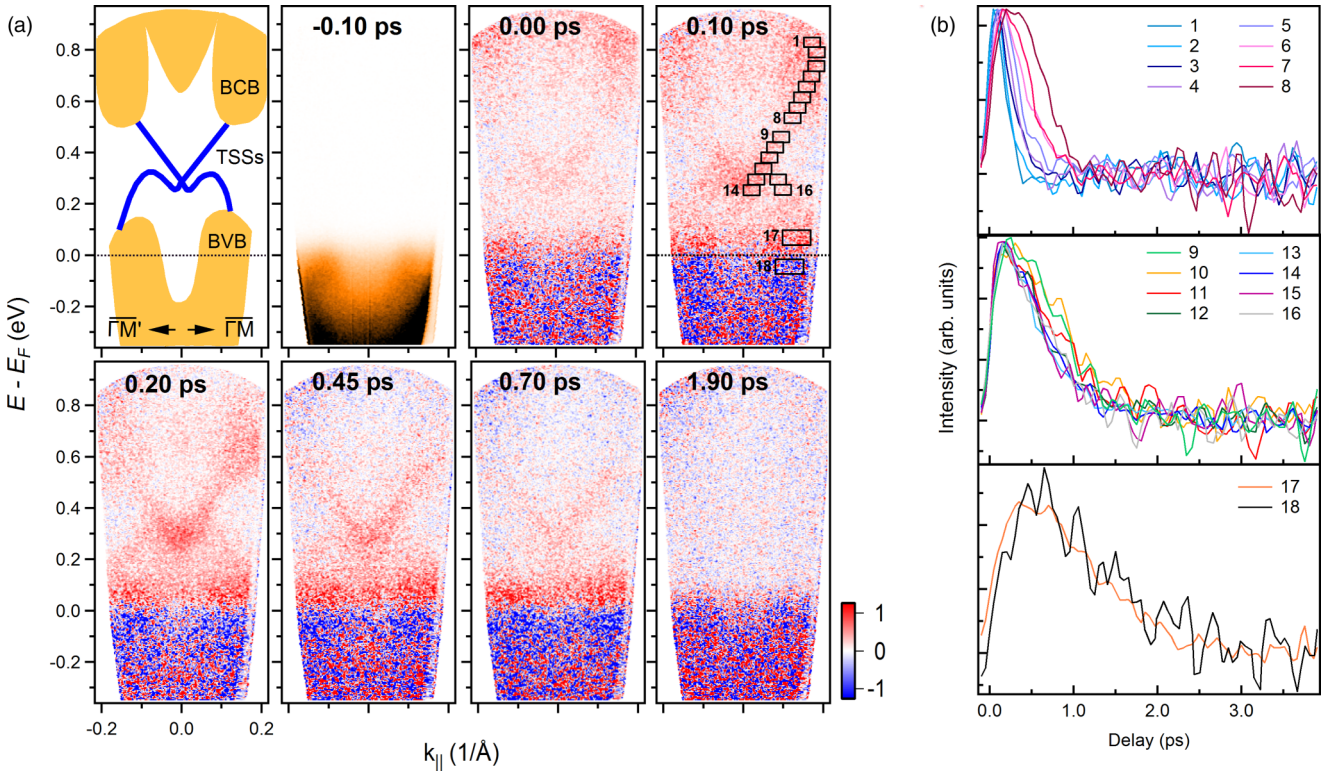

FIG. 4. Ultrafast dynamics the photoexcited electronic states. (a) In the upper-left corner, we exhibit a schematic view of the electronic band structure of the Te-rich terminated region along $\overline{\Gamma M}$–$\overline{\Gamma M'}$. Excess electron (red) and hole (blue) populations are detected from the difference time-resolved ARPES images obtained before and after photoexcitation. Dashed lines indicate the Fermi level. (b) Ultrafast time evolution of the populations in the k-E integration windows 1–18 presented at $t = 0.10$ ps pump-probe delay.

playing a key role. In particular, the electron-phonon coupling seems stronger than for 3D TIs, since for this system the TSSs do not present the markedly longer lifetime with respect to the bulk bands observed in prototype materials like Bi_2Se_3 and Bi_2Te_3 [9,27,28]. In fact, since this system is a semimetal, the phase space available for electrons to relax is much wider than the one available in Bi_2Se_3 and Bi_2Te_3, making possible for electrons to couple with a large number of available phonons.

Since the trARPES yield is essentially representative of the Te-rich QL termination, this means that the results presented in Fig. 4 correspond to a Sb_2Te_3 surface slab [see Fig. 1(a)]. If one compares our data with the corresponding data for Sb_2Te_3 [15,16], it is clear that the surface electronic structure of "Sb_2Te_3-terminated" $SbTe_2$ is markedly different from Sb_2Te_3, in particular for the TSSs. This confirms that, as in the case of Bi_4Se_3 [18], it is the bulk band structure that determines the TSSs, not the structure of the first quintuple layer of the host. Furthermore, the dynamics presented in Fig. 4 indicate a strong coupling between surface states and bulk, which can be explained by a penetration depth of the Dirac state of more than a structural unit slab, consistent to what is found for prototype materials like Bi_2Te_3 [25] and more recently for other topological insulators like $SnSb_2Te_4$ [29].

IV. CONCLUSION

In conclusion, we performed a combined μ-ARPES and trARPES study of the natural topological superlattice phase Sb_2Te. Our μ-ARPES results clearly show that three distinct types of surface termination can coexist after cleaving a single crystal of this material, each one presenting a different surface and bulk band dispersion. Based on this microscopic analysis, we can also conclude that the preponderant termination is the Te-rich one, that we were able study also by means of trARPES. The analysis of the transient electronic structure for the TSSs and bulk bands along high-symmetry directions in the Brillouin zone shows that the TSSs of "Sb_2Te_3-terminated" Sb_2Te are considerably different from simple Sb_2Te_3, confirming that the surface properties of topological multilayers are determined by more than one structural unit. Further theoretical efforts, taking into account all these factors, are required to understand in detail the interplay between multilayer structures and surface electronic properties of this new class of topological materials.

ACKNOWLEDGMENTS

We acknowledge financial support by the RTRA Triangle de la Physique, the EU/FP7, under the Go Fast program (Grant No. 280555), by "Investissement d'Avenir" Labex PALM (ANR-10-LABX-0039-PALM), by the Equipex ATTOLAB (ANR11-EQPX0005-ATTOLAB), and by the ANR Iridoti (Grant No. ANR-13-IS04-0001). Research at Princeton University was supported by the US National Science Foundation through the MRSEC program, Grant No. DMR-1420451.

[1] M. Z. Hasan and C. L. Kane, Rev. Mod. Phys. **82**, 3045 (2010).
[2] J. E. Moore, Nature (London) **464**, 194 (2010).
[3] X.-L. Qi and S.-C. Zhang, Rev. Mod. Phys. **83**, 1057 (2011).
[4] A. Bansil, H. Lin, and T. Das, Rev. Mod. Phys. **88**, 021004 (2016).
[5] Y. Xia, D. Qian, D. Hsieh, L. Wray, A. Pal, H. Lin, A. Bansil, D. Grauer, Y. S. Hor, R. J. Cava, and M. Z. Hasan, Nat. Phys. **5**, 398 (2009).
[6] H. Zhang, C.-X. Liu, X.-L. Qi, X. Dai, Z. Fang, and S.-C. Zhang, Nat. Phys. **5**, 438 (2009).
[7] P. Roushan, J. Seo, C. V. Parker, Y. S. Hor, D. Hsieh, D. Qian, A. Richardella, M. Z. Hasan, R. J. Cava, and A. Yazdani, Nature (London) **460**, 1106 (2009).
[8] J. Seo, P. Roushan, H. Beidenkopf, Y. S. Hor, R. J. Cava, and A. Yazdani, Nature (London) **466**, 343 (2010).
[9] Y. Wang, F. Xiu, L. Cheng, L. He, M. Lang, J. Tang, X. Kou, X. Yu, X. Jiang, Z. Chen, J. Zou, and K. L. Wang, Nano Lett. **12**, 1170 (2012).
[10] A. A. Burkov and L. Balents, Phys. Rev. Lett. **107**, 127205 (2011).
[11] H. Jin, J. Im, J.-H. Song, and A. J. Freeman, Phys. Rev. B **85**, 045307 (2012).
[12] J. C. Johannsen, G. Autès, A. Crepaldi, S. Moser, B. Casarin, F. Cilento, M. Zacchigna, H. Berger, A. Magrez, P. Bugnon, J. Avila, M. C. Asensio, F. Parmigiani, O. V. Yazyev, and M. Grioni, Phys. Rev. B **91**, 201101(R) (2015).
[13] V. Agafonov, N. Rodier, R. Céolin, R. Bellissent, C. Bergman, and J. P. Gaspard, Acta Crystallogr., Sect. C: Cryst. Struct. Commun. **47**, 1141 (1991).
[14] H. Luo, Q. Gibson, J. Krizan, and R. J. Cava, J. Phys.: Condens. Matter **26**, 206002 (2014).
[15] J. Reimann, J. Güdde, K. Kuroda, E. V. Chulkov, and U. Höfer, Phys. Rev. B **90**, 081106(R) (2014).
[16] S. Zhu, Y. Ishida, K. Kuroda, K. Sumida, M. Ye, J. Wang, H. Pan, M. Taniguchi, S. Qiao, S. Shin, and A. Kimura, Sci. Rep. **5**, 13213 (2015).
[17] D. Hsieh, Y. Xia, D. Qian, L. Wray, F. Meier, J. H. Dil, J. Osterwalder, L. Patthey, A. V. Fedorov, H. Lin, A. Bansil, D. Grauer, Y. S. Hor, R. J. Cava, and M. Z. Hasan, Phys. Rev. Lett. **103**, 146401 (2009).
[18] Q. D. Gibson, L. M. Schoop, A. P. Weber, H. Ji, S. Nadj-Perge, I. K. Drozdov, H. Beidenkopf, J. T. Sadowski, A. Fedorov, A. Yazdani, T. Valla, and R. J. Cava, Phys. Rev. B **88**, 081108(R) (2013).
[19] P. Dudin, P. Lacovig, C. Fava, E. Nicolini, A. Bianco, G. Cautero, and A. Barinov, J. Synchrotron Radiat. **17**, 445 (2010).
[20] J. Faure, J. Mauchain, E. Papalazarou, W. Yan, J. Pinon, M. Marsi, and L. Perfetti, Rev. Sci. Instrum. **83**, 043109 (2012).
[21] E. Papalazarou, J. Faure, J. Mauchain, M. Marsi, A. Taleb-Ibrahimi, I. Reshetnyak, A. van Roekeghem, I. Timrov, N. Vast, B. Arnaud, and L. Perfetti, Phys. Rev. Lett. **108**, 256808 (2012).
[22] G. Lantz, M. Hajlaoui, E. Papalazarou, V. L. R. Jacques, A. Mazzotti, M. Marsi, S. Lupi, M. Amati, L. Gregoratti, L. Si, Z. Zhong, and K. Held, Phys. Rev. Lett. **115**, 236802 (2015).
[23] L. Gregoratti, S. Günther, J. Kovac, M. Marsi, R. J. Phaneuf, and M. Kiskinova, Phys. Rev. B **59**, 2018 (1999).
[24] M. Marsi, L. Casalis, L. Gregoratti, S. Günther, A. Kolmakov, J. Kovac, D. Lonza, and M. Kiskinova, J. Electron Spectrosc. Relat. Phenom. **84**, 73 (1997).
[25] M. Hajlaoui, E. Papalazarou, J. Mauchain, G. Lantz, N. Moisan, D. Boschetto, Z. Jiang, I. Miotkowski, Y. P. Chen, A. Taleb-Ibrahimi, L. Perfetti, and M. Marsi, Nano Lett. **12**, 3532 (2012).
[26] J. A. Sobota, S. Yang, J. G. Analytis, Y. L. Chen, I. R. Fisher, P. S. Kirchmann, and Z.-X. Shen, Phys. Rev. Lett. **108**, 117403 (2012).
[27] J. A. Sobota, S.-L. Yang, A. F. Kemper, J. J. Lee, F. T. Schmitt, W. Li, R. G. Moore, J. G. Analytis, I. R. Fisher, P. S. Kirchmann, T. P. Devereaux, and Z.-X. Shen, Phys. Rev. Lett. **111**, 136802 (2013).
[28] M. Hajlaoui, E. Papalazarou, J. Mauchain, L. Perfetti, A. Taleb-Ibrahimi, F. Navarin, M. Monteverde, P. Auban-Senzier, C. R. Pasquier, N. Moisan *et al.*, Nat. Commun. **5**, 3003 (2014).
[29] D. Niesner, S. Otto, V. Hermann, T. Fauster, T. V. Menshchikova, S. V. Eremeev, Z. S. Aliev, I. R. Amiraslanov, M. B. Babanly, P. M. Echenique, and E. V. Chulkov, Phys. Rev. B **89**, 081404(R) (2014).